Clean Air, Vol. 5, pp. 21–44, 2004

CATALYTIC COMBUSTION OF HYDROGEN–AIR MIXTURES OVER PLATINUM: VALIDATION OF HETERO/HOMOGENEOUS CHEMICAL REACTION SCHEMES

C. APPEL, J. MANTZARAS*, R. SCHAEREN, R. BOMBACH,

and A. INAUEN

Paul Scherrer Institute, Combustion Research, CH-5232 Villigen-PSI, Switzerland

The validity of various hetero/homogeneous chemical reaction schemes in the catalytically stabilized combustion (CST) of hydrogen/air mixtures over platinum is investigated experimentally and numerically. The work stems from the internationally intensified effort to commercialize power generation turbines operating with the ultra-low NO_x CST technology. Crucial to the development of such systems is the understanding of the heterogeneous (catalytic) and the homogeneous (gas-phase) kinetics. Experiments were performed in an optically accessible catalytic channel reactor and involved planar laser induced fluorescence (PLIF) of the OH radical and line-Raman measurements of major species concentrations. The comparisons between measurements and detailed numerical predictions using elementary, reduced, or one-step mechanisms have revealed substantial differences in the performance of the reaction schemes.

Keywords: catalytically stabilized combustion modeling; homogeneous ignition; planar laser induced fluorescence; 1-D Raman

INTRODUCTION

Catalytically stabilized combustion (CST) provides the best available low-NO_x combustion technology, with demonstrated NO_x emissions less than 3 ppm (Beebe, 2000). In CST partial fuel conversion is attained catalytically (heterogeneously) and the remaining fuel is combusted in a follow-up homogeneous (gas-phase) combustion zone. The heterogeneous combustion is a flameless process and does not contribute to NO_x, which is formed only via the homogeneous reaction pathway. CST is, therefore, a NO_x-preventing technology, resulting in a significant cost reduction compared to NO_x-aftertreatment techniques (SCR or SCONOX). The CST research activities are internationally intensified, driven by the stringent NO_x emission regulations in Europe and the United States (non-attainment areas in the United States already impose a 3 ppm NO_x limit). CST has

*Address all correspondence to J. Mantzaras, ioannis.mantzaras@psi.ch.

been recently commercialized in small-scale (1.5 MW) gas turbines in the United States and current efforts focus on large-scale machines.

Further advancement in CST technology requires the development of catalysts with improved activity (desired light-off temperature less than 450^{o}C) and thermal stability, understanding of the catalytic surface processes, knowledge of low- temperature homogeneous kinetics and their respective coupling with heterogeneous kinetics. The catalytic reactor in power generation systems consists of a multitude of large surface-to-volume ratio catalytically coated channels, necessitating multidimensional numerical models with capabilities of detailed hetero/homogeneous chemistry, transport, and flow description. These models could be used to predict issues of practical interest, such as light-off characteristics, the likelihood of homogeneous ignition, and the attained fuel conversion within the catalytic reactor.

Heterogeneous kinetic studies of simple fuels such as H_2, CO and CH_4 over Pt or Pd have progressed substantially over the last years, *e.g.*, Hellsing *et al.* (1991), Hickman and Schmidt (1993), Deutschmann (1996), and Aghalayam *et al.* (2000). In addition, multidimensional numerical models capable of treating detailed surface and gas-phase kinetics are now available (refer to Dogwiler (1998), Deutschmann and Schmidt (1998)). The onset of homogeneous ignition within the catalytic reactor is detrimental to the catalyst integrity (it can cause catalyst meltdown) and the knowledge of such an event is of prime interest to CST reactor design. The gas-phase ignition is strongly influenced by the hetero/homogeneous coupling (catalytic fuel depletion, radical adsorption/desorption reactions) and, therefore, its accurate prediction requires the use of validated hetero/homogeneous chemical reaction schemes. In Dogwiler (1998) and Dogwiler *et al.* (1999), the authors validated hetero/homogeneous reaction schemes in CST of CH_4/air mixtures over Pt, using a 2-D elliptic fluid mechanical model with elementary hetero/homogeneous reaction schemes and experimental ignition characteristics from an optically accessible catalytic combustor. Mantzaras and Benz (1999) have provided analytical homogeneous ignition criteria in 2-D channel configurations that included dependencies on the relevant chemical, flow, transport, and geometrical parameters. Such criteria were further adapted to CH_4/air CST in Mantzaras et al. (2000a) using the validated hetero/homogeneous schemes from Dogwiler (1998).

Of particular interest in natural gas-fueled turbines is the concept of hydrogen-assisted CST. Addition of small amounts of H_2 in natural gas reduces the catalyst light-off temperature and improves the combustion stability by damping flame pulsations. Dobbeling and Griffin (1999) proposed partial catalytic oxidation of a fraction of the natural gas as a viable way of producing hydrogen in gas-turbine systems. The knowledge of hydrogen CST is, therefore, an important step in the understanding of hydrogen-assisted CST. In hydrogen-assisted CST, care has

to be exercised to avoid catalyst hot-spots and homogeneous ignition within the catalytic reactor: H_2 is a strongly diffusionally imbalanced fuel with a Lewis number Le ≈ 0.3, resulting in superadiabatic surface temperatures (see Pfefferle and Pfefferle, 1985), that could deactivate the catalyst and promote homogeneous ignition.

In this article we investigate experimentally and numerically the CST of fuel-lean H_2/air mixtures over Pt in laminar channel flows. Experiments have been performed at atmospheric pressure in a catalytic channel combustor formed by two Pt-coated parallel ceramic plates. Planar laser induced fluorescence (PLIF) of the OH radical along the streamwise plane of symmetry monitored the onset of homogeneous ignition, line-Raman (across the channel transverse direction) provided the boundary layer profiles of the major species and temperature, and thermocouples embedded beneath the catalyst surfaces yielded the catalyst temperature distribution. Numerical simulations were performed with a 2-D elliptic fluid mechanical model that included multicomponent transport and hetero/homogeneous chemical description. In the homogeneous chemistry, six schemes were evaluated: three elementary schemes, one reduced and two single-step ones. In the heterogeneous chemistry, two elementary and one single-step scheme were evaluated. The objective was to validate the CST-applicability of the aforementioned hetero/homogeneous schemes. The inclusion of reduced and single-step reaction schemes complements our recent evaluation of elementary hetero/homogeneous schemes (Appel, 2002).

EXPERIMENTAL

Burner Geometry

The catalytic channel reactor consisted of two horizontal Si[SiC] ceramic plates, 300 mm long (L), 110 mm wide and 10 mm thick, placed 7 mm ($2b$) apart (see Figure 1). Two vertical quartz windows 300 mm long, 12 mm high and 3 mm thick, with a corresponding lateral window separation of 104 mm (W), completed the channel enclosure (see Figure 1b). The reactor was delineated by the $L \times W \times 2b$ volume. Optical accessibility was provided from both 300 mm × 7 mm sides, excluding two 18-mm long sections near the channel center blocked by window-support metal elements. The inner surfaces of the ceramic plates were coated with a layer of 1.5-μm thick nonporous Al_2O_3 followed by a 2.2-μm platinum layer; both layers were applied with Plasma Vapor Deposition (PVD), resulting in uniform Pt surface distribution and good adhesion and thermal stability of both Al_2O_3 and Pt. The catalyst surface temperature was monitored along the x–y

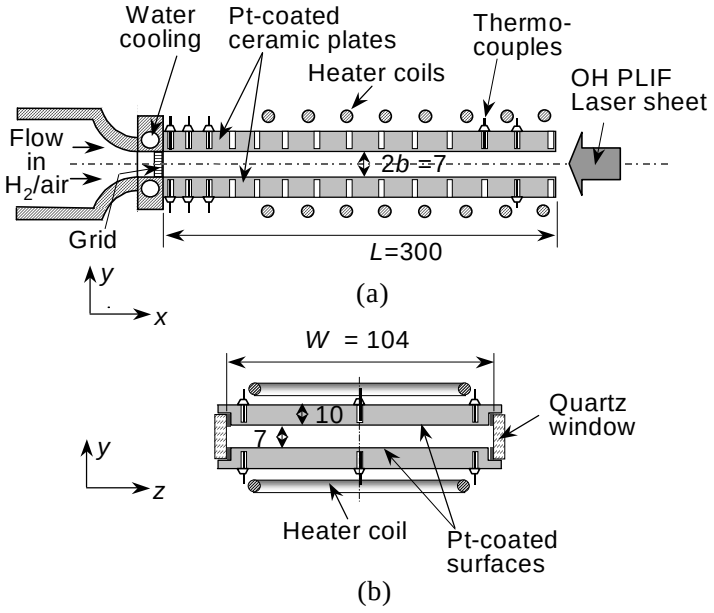

FIGURE 1 Schematic of the test-rig: (a) streamwise view, (b) lateral view. All distances are in mm.

symmetry plane (z = 0) with S-thermocouples (14 for each plate) embedded 0.9 mm beneath the Pt-coated surfaces through holes eroded from the outer plate sides. Given the high thermal conductivity of Si[SiC] (~35 $W \cdot m^{-1} \cdot K^{-1}$), the thermocouple measurements reflected accurately the actual catalyst surface temperature. The absolute difference between top and bottom plate temperature distributions was, at any given x-location, less than 6 K. Additional side-thermocouples were positioned at $z = \pm 40$ mm and x = 22, 110 mm. The combustor was positioned inside an inconel-steel frame and the entire test-rig was mounted on an optical table traversable in the x-direction to facilitate the Raman experiments.

In fuel-lean H_2/air CST, the catalyst can reach superadiabatic temperatures: as shown in Bui, Vlachos, and Westmoreland (1996), the diffusional imbalance of H_2 results in a surface equivalence ratio about twice that of the gas phase. Moreover, the highest surface temperatures are attained at the channel entry, as shown in Pfefferle and Pfefferle (1985). Experiments in the combustor of Figure 1 under such conditions led to a gaseous flame anchored directly at the hot entrance. To suppress the high catalyst entry temperatures and, at the same time, to maintain gaseous combustion, a combined cooling/heating arrangement was adopted. The 110 mm $\times$ 10 mm entry sides of the catalytic plates were contacted to a water-cooled section of the metal frame (see Figure 1a). In addition, the last 240 mm of both ceramic plates were resistively heated with two 2.5-kW heaters. The ex-

Table I Experimental conditions (inlet velocity, Reynolds number, inlet temperature, and equivalence ratio)

Case	U_{IN} (m/s)	Re_{IN}	T_{IN} (K)	φ
1	1.6	1100	313	0.28
2	1.6	1090	313	0.32
3	2.0	1390	312	0.28
4	2.0	1370	312	0.32
5	3.0	2080	312	0.28
6	3.0	2060	312	0.32

ternal heating was necessary to counteract heat losses, which were significant under the present low flow-rate laminar experiments.

The H_2 and air flow rates were measured with two Brooks mass flow controllers, mixed in two sequential Sulzer static mixers, passed through a section filled with 2-mm diameter metallic spheres to straighten the flow and, finally, were brought to the combustor through an entry section with an ending *y*-contraction ratio of 3:1. A 2-mm long metal grid (1 mm^2 mesh) was positioned on the water-cooled frame just upstream of the catalyst, to maintain uniform inlet temperature and velocity profiles. A retractable thermocouple positioned downstream of the metal grid monitored the inlet temperature. The open side of the exhaust side allowed for additional optical access, through which the OH PLIF laser sheet (see Figure 1a) was introduced into the combustor. All atmospheric-pressure experiments were performed at laminar flow conditions; the experimental conditions are given in Table I. The Reynolds numbers of Table I were based on the inlet properties and the channel hydraulic diameter (= 13.1 mm). The adiabatic flame temperatures were 1149.4 K (φ = 0.28) and 1249.5 K (φ = 0.32).

Laser Diagnostics

The OH PLIF and Raman setup is illustrated in Figure 2. In the PLIF experiment, a frequency-doubled Nd:YAG pulsed laser (Quantel YG781C20) pumped a tunable dye laser (Quantel TDL50) with a resulting radiation at 285.09 nm. The laser beam was transformed into a vertical laser sheet that propagated in a counterflow direction along the *x*–*y* symmetry plane from the burner's exhaust side. Optical accessibility to the catalytic wall surfaces was assured by inducing a small beam divergence in the *y*-direction. The fluorescence from both (1–1) and (0–0) transitions, at 308 nm and 314 nm respectively, was collected at 90^o angle through one of the quartz windows with an intensified CCD camera (LaVision FlameStar 2F, 576 × 384 pixels). One hundred images were averaged to increase the signal to noise ratio. The PLIF was calibrated with absorption measurements

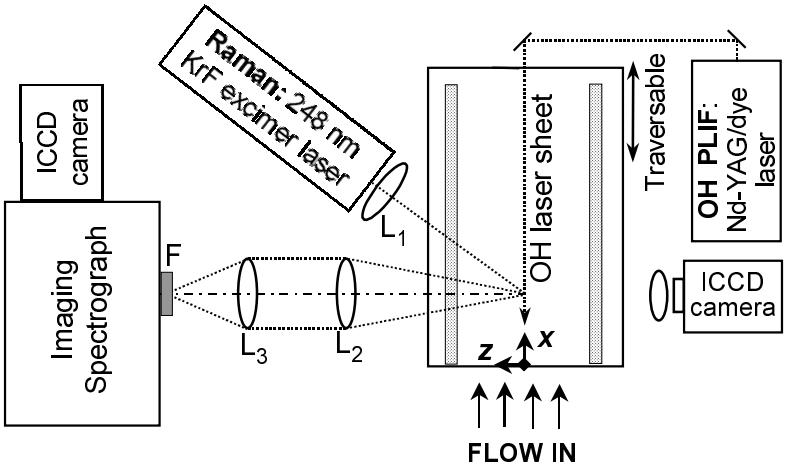

FIGURE 2 Schematic of the OH PLIF and Raman setup.

performed with the laser sheet crossing laterally (*z*-direction) through both quartz windows.

In the Raman measurements, a two-stage tunable narrowband KrF excimer laser (Lambda Physik Compex 150 T) was used. The pulse energy was 230 mJ at 248 nm. The rectangular, 25 mm × 9 mm cross section, excimer beam was focused to a vertical line (0.3-mm thick) inside the combustor by an f_1 = 202 mm cylindrical quartz lens (L_1). The focal line spanned the 7-mm transverse channel distance and was offset laterally (z = 15 mm) to increase the collection angle and minimize beam steering effects. As the combustion was strongly two-dimensional with no lateral dependence (except in regions extending up to ~15 mm from the quartz windows), this offset did not affect the forthcoming comparisons with the 2-D numerical predictions. Two quartz lenses (L_2 and L_3) with f_2 = 200 mm and f_3 = 300 mm, respectively, focused the Raman scattered light to the entrance slit of a 25-cm imaging spectrograph (Chromex 250i). A second intensified CCD camera, same to that of the PLIF setup, recorded the dispersed spectra; the two dimensions of the CCD chip corresponded to spectral shift and *y*-distance. The spectral dispersion on the CCD camera ranged from 1250 cm^{-1} to 5000 cm^{-1} allowing observation of all major species: O_2, N_2, H_2O, and H_2. The vibrational structure of each species spectrum was not resolved and the temperature was determined by the N_2 line. Determination of the effective Raman cross sections, which included transmission efficiencies, *e.g.*, windows, lenses, filter, spectrometer and camera, was accomplished by recording the Raman signals of pure H_2, air, and exhaust gases of known composition (the latter for assessing the cross section of H_2O). Notwithstanding the care in tuning the KrF laser wavelength, fluorescence contributions from oxygen hot-bands disturbed significantly the Raman oxy-

gen signals. Therefore, quantitative O_2 concentrations were not deduced. The 250 pixel transverse extent was binned to 27 pixels, yielding a *y*-resolution of 0.26 mm. Raman measurements closer than 0.6 mm from both walls were rejected due to low signal-to-noise ratio.

NUMERICAL MODEL

The governing set of equations for a 2-D steady, laminar reactive flow with homogeneous and heterogeneous chemical reactions are:

Continuity equation:

$$\frac{\partial(\rho u)}{\partial x}+\frac{\partial(\rho v)}{\partial y}=0 \tag{1}$$

Momentum equations:

$$\frac{\partial(\rho uu)}{\partial x}+\frac{\partial(\rho vu)}{\partial y}+\frac{\partial p}{\partial x}-\frac{\partial}{\partial x}\left[2\mu\frac{\partial u}{\partial x}-\frac{2}{3}\mu\left(\frac{\partial u}{\partial x}+\frac{\partial v}{\partial y}\right)\right]-\frac{\partial}{\partial y}\left[\mu\left(\frac{\partial u}{\partial y}+\frac{\partial v}{\partial x}\right)\right]=0 \tag{2}$$

$$\frac{\partial(\rho uv)}{\partial x}+\frac{\partial(\rho vv)}{\partial y}+\frac{\partial p}{\partial y}-\frac{\partial}{\partial x}\left[\mu\left(\frac{\partial v}{\partial x}+\frac{\partial u}{\partial y}\right)\right]-\frac{\partial}{\partial y}\left[2\mu\frac{\partial v}{\partial y}-\frac{2}{3}\mu\left(\frac{\partial u}{\partial x}+\frac{\partial v}{\partial y}\right)\right]=0 \tag{3}$$

Energy equation:

$$\frac{\partial(\rho uh)}{\partial x}+\frac{\partial(\rho vh)}{\partial y}+\frac{\partial}{\partial x}\left(\rho\sum_{k=1}^{Kg}Y_k h_k V_{k,x}-\lambda\frac{\partial T}{\partial x}\right)+\frac{\partial}{\partial y}\left(\rho\sum_{k=1}^{Kg}Y_k h_k V_{k,y}-\lambda\frac{\partial T}{\partial y}\right)=0 \tag{4}$$

Gas phase species equations:

$$\frac{\partial(\rho uY_k)}{\partial x}+\frac{\partial(\rho vY_k)}{\partial y}+\frac{\partial}{\partial x}\left(\rho Y_k V_{k,x}\right)+\frac{\partial}{\partial y}\left(\rho Y_k V_{k,y}\right)-\dot{w}_k W_k=0 \tag{5}$$

$k = 1, 2, ..., K_g$

Surface species coverage equations:

$$\frac{\partial\Theta_m}{\partial t}=\sigma_m\frac{\dot{s}_m}{\Gamma}-\frac{\Theta_m}{\Gamma}\dot{\Gamma} \tag{6}$$

$m = 1, 2, ..., M_S$.

The species diffusion velocities $\vec{V}_k$ were determined from the full multicomponent diffusion equation:

$$\nabla X_k = \sum_{\ell=1}^{K_g} \frac{X_k X_\ell}{D_{k\ell}} \left(\vec{V}_\ell - \vec{V}_k\right) + \left(Y_k - X_k\right) \frac{\nabla p}{p} + \sum_{\ell=1}^{K_g} \frac{X_k X_\ell}{\rho D_{k\ell}} \left(\frac{D_\ell^T}{Y_\ell} - \frac{D_k^T}{Y_k} \right) \frac{\nabla T}{T} \tag{7}$$

$k = 1, 2, ..., K_g$.

Finally, the ideal gas and caloric equations of state were:

$$p = \rho RT/\overline{W} \quad \text{and} \quad h_k = h_k^o(T_o) + \int_{T_O}^{T} c_{p,k}\, dT \tag{8}$$

respectively. The set of equations (1)–(8) was solved subject to the following boundary conditions. At the gas–wall interface ($y = 0$), the energy and gas-phase species boundary conditions were:

$$T\big|_{y=0} = T_W(x) \quad \text{and} \quad (\rho Y_k V_{k,y})_{y=0} = W_k \dot{s}_k\,, \tag{9}$$

respectively, with $T_W(x)$ the average (over both plates) thermocouple-measured temperature distribution. The inlet conditions were uniform profiles for the temperature, the axial velocity, and the species compositions. Zero-Neumann conditions were applied at the exit and the symmetry plane ($y = b$). Up to 340 × 90 grid points were used to resolve a 250 mm × 3.5 mm channel domain (in x and y respectively). The multicomponent transport of equation (7) (including thermal diffusion) was implemented in a fashion similar to Kuijlaars, Kleijn, and van den Akker (1995) to avoid matrix inversion. Finally, the solution was obtained iteratively with a Simpler-based finite volume method and time-splitting between gaseous and surface treatment; details are given in Dogwiler *et al.* (1999) and Mantzaras (2000b).

CHEMICAL KINETICS

Homogeneous Chemical Reaction Schemes

Six gas-phase mechanisms were investigated. Firstly, the global reaction $H_2 + 1/2\ O_2 \rightarrow H_2O$ was considered, with the one-step mechanisms of Mitani and Williams (1980):

$$R = A C_{H_2} C_{O_2} \exp\left(-E/RT\right), \tag{10}$$

with $A = 2.196 \times 10^{12}$ mol^{-1}·cm^3·s^{-1}, $E = 109.2$ kJ/mol, and Marinov, Westbrook, and Pitz (1995):

Table II Summary of homogeneous reaction schemes

Notation of gaseous schemes	Type	Reference
Mitani	One-step	Mitani and Williams (1980), equation (10)
Marinov	One-step	Marinov, Westbrook, and Pitz (1995), equation (11)
Seshadri	Two-step reduced	Seshadri, Peters, and Williams (1994), equation (12)
Warnatz	Elementary	Warnatz and Maas (1993), 9 reversible reactions
Yetter	Elementary	Mueller (1999), 23 reversible reactions
Miller	Elementary	Miller and Bowman (1989), 20 reversible reactions

$$R = AC_{H_2}C_{O_2}^{0.5} \exp(-E/RT), \tag{11}$$

with $A = 1.8 \times 10^{13}$ $mol^{-0.5} \cdot cm^{1.5} \cdot s^{-1}$ and $E = 146.4$ kJ/mol. The reduced mechanism from Seshadri, Peters, and Williams (1994) was also investigated, consisting of two steps involving the species H_2, O_2, H_2O, and H:

$$3\ H_2 + O_2 = 2H_2O + 2H\ ,$$

$$2\ H + M = H_2 + M\ , \tag{12}$$

and algebraic relations for the steady-state concentrations of HO_2, O and OH. Expressions for the global reaction rate constants of reactions (12) and the algebraic relations for the steady-state species are given in Seshadri *et al.* (1994). Finally, three elementary mechanisms of the H/O system involving eight species were investigated, further denoted as Warnatz (Warnatz and Maas, 1993), Yetter (Mueller, 1999), and Miller (Miller and Bowman, 1989). Table II summarizes all homogeneous schemes.

Heterogeneous Chemical Reaction Schemes

The one-step mechanism of Schefer (1982) is:

$$R = AC_{H_2} \exp(-E/RT), \tag{13}$$

with $A = 1.4 \times 10^3$ cm/s and $E = 14.9$ kJ/mol. Two elementary heterogeneous schemes were additionally studied, further denoted as Warnatz (Deutschmann, 1996) and Kasemo (Hellsing *et al.*, 1991). The elementary schemes are shown in Table III. In Warnatz's scheme, the H_2 adsorption is first order with respect to Pt, the oxygen sticking coefficient is temperature dependent, $\gamma_{O_2} = 0.07(T_o/T)$ with $T_o = 300$ K and reactions (8), (10), and (12) are calculated from the forward rates (7), (9), and (11) and the surface thermochemical data of Warnatz (1994). In Kasemo's scheme, the H_2 adsorption was also first order with respect to Pt. Kasemo's scheme has been augmented with the addition of radical (O, H, and

Table III Elementary heterogeneous schemes

	Reactions (a)	Warnatz		Kasemo	
	Adsorption reactions	$A(\gamma)$	E	$A(\gamma)$	E
1	$H_2 + 2Pt(s) \rightarrow 2H(s)$	0.046	–	0.046	–
2	$H + Pt(s) \rightarrow H(s)$	1.0	–	1.0	–
3	$O_2 + 2Pt(s) \rightarrow 2O(s)$	0.07	–	0.023	–
4	$O + Pt(s) \rightarrow O(s)$	1.0	–	1.0	–
5	$H_2O + Pt(s) \rightarrow H_2O(s)$	0.75	–	0.70	–
6	$OH + Pt(s) \rightarrow OH(s)$	1.0	–	1.0	–
	Surface reactions				
7	$H(s) + O(s) \rightarrow OH(s) + Pt(s)$	3.7×10^{21}	11.5	3.7×10^{21}	11.5
8	$OH(s) + Pt(s) \rightarrow H(s) + O(s)$	(b)		3.7×10^{21}	24.5
9	$H(s) + OH(s) \rightarrow H_2O(s) + Pt(s)$	3.7×10^{21}	17.5	3.7×10^{21}	17.5
10	$H_2O(s) + Pt(s) \rightarrow H(s) + OH(s)$	(b)		3.7×10^{21}	113.5
11	$OH(s) + OH(s) \rightarrow H_2O(s) + O(s)$	3.7×10^{21}	48.2	3.7×10^{21}	48.2
12	$H_2O(s) + O(s) \rightarrow OH(s) + OH(s)$	(b)		3.7×10^{21}	131.4
	Desorption reactions				
13	$2H(s) \rightarrow H_2 + 2Pt(s)$	3.7×10^{21}	$67.4 - 6\Theta_H$	3.7×10^{21}	67.4
14	$2O(s) \rightarrow O_2 + 2Pt(s)$	3.7×10^{21}	$213.2 - 60\Theta_O$	3.7×10^{21}	213.2
15	$H_2O(s) \rightarrow H_2O + Pt(s)$	10^{13}	40.3	10^{13}	42.3
16	$OH(s) \rightarrow OH + Pt(s)$	10^{13}	192.8	10^{13}	192.8

(a)A [mol·cm·K·s] and E [kJoule/mole], except in adsorption reactions where A is a sticking coefficient (γ).

(b)Calculated from forward rates and surface thermodata.

Table IV Summary of heterogeneous schemes

Notation of heterogeneous schemes	Type	Reference
Schefer	One-step	Schefer (1982), (equation (13))
Warnatz	Elementary	Deutschmann (1996), (Table III)
Kasemo	Elementary	Hellsing, Kasemo, and Zhdanov (1991), (Table III)

OH) adsorption reactions with sticking coefficients of unity, as in Warnatz's scheme. These reactions were necessary for accurate homogeneous ignition predictions as will be further discussed in the results section; it is noted that the scheme of Kasemo was originally tested in processes without gas-phase combustion where the absence of radical adsorption reactions was justified.

All heterogeneous schemes are summarized in Table IV. The surface site density was taken as $\Gamma = 2.7 \times 10^{-9}$ mol/cm^2, simulating polycrystalline platinum: the thick (2.2 μm) Pt layer on top of a non-porous Al_2O_3 layer closely resembled such a surface. Gas phase and surface reaction rates were evaluated with Chemkin and surface Chemkin respectively. Finally, the Chemkin database was used for the gas-phase thermochemical and transport properties (Kee, 1996).

RESULTS AND DISCUSSION

Investigation of Homogeneous Reaction Pathway

Typical thermocouple-measured streamwise surface temperature profiles are shown in Figure 3. The efficient water-cooling of the entry section led to suppression of the otherwise high entry temperatures. Moreover, the surface temperatures were at most 110 K (case 1) higher than the respective adiabatic flame temperatures. Increasing U_{IN} resulted in lower temperatures at $x \geq 100$ mm, due to a corresponding reduction in the power of the heaters with increasing case number. PLIF-measured 2-D distributions of the OH concentrations are illustrated in Figure 4 (Case 4) along with corresponding numerical predictions. The predictions refer to the heterogeneous scheme of Warnatz and the elementary or reduced homogeneous schemes of Table II. The onset of homogeneous ignition (shown with arrows in Figure 4) is determined as follows. Figure 5a presents the streamwise catalytic fuel conversion (C), the gaseous (G) fuel conversion, and the OH mole fraction (the last two integrated over $y = b$). The sharp rise in either the OH or G profiles

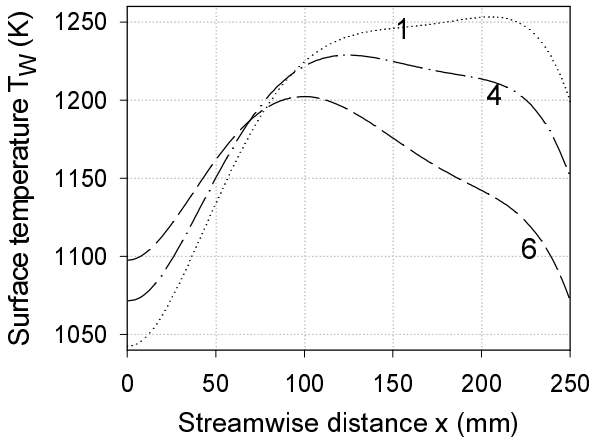

FIGURE 3 Measured surface temperature distributions for cases 1, 4, and 6 of Table I.

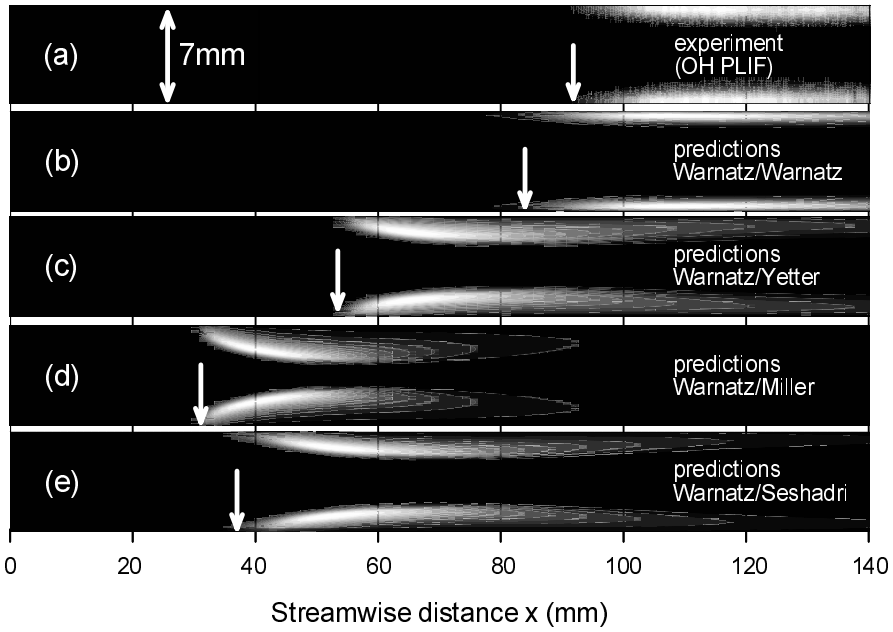

FIGURE 4 Measured (panel a) and predicted (panels b–e) OH distributions for case 4. White corresponds to high OH intensity and black to low; the intensity scale is different in each panel. In panels (b) to (e) the first reaction-mechanism-entry refers to the heterogeneous pathway and the second one to the homogeneous pathway. The arrows indicate the homogeneous ignition locations.

can be alternatively used to define homogeneous ignition: the intersection of the tangent to the inflection point of the OH profile with the *x*-axis determined the ignition distances (x_{ig}) in both experiments and predictions.

As shown in Figure 4, there were substantial differences between measured and predicted homogeneous ignition distances: the gaseous scheme of Warnatz gave the best agreement (8% underprediction), Yetter's underprediction was 43%, Miller's was 67%, and Seshadri's was 50%. All other cases of Table IV exhibited similar discrepancies. To understand the origin of the ignition differences, sensitivity analysis was performed for all elementary homogeneous schemes. The preexponential constant of each gaseous reaction was multiplied or divided by a given factor K, and the x_{ig} were recomputed. The unaltered heterogeneous scheme of Warnatz was used in this analysis. Factors K of 1.2, 1.5, and 2 produced the same set of significant reactions. Figure 6 illustrates the percentage change in ignition distance for the five most important reactions and for a multiplication (black bars) or division (grey bars) factor of two. In all homogeneous schemes, the most sensitive reactions had the same order of significance. The two most important reactions in all schemes were the chain branching $H + O_2 = O + OH$ (R1) and terminating $H + O_2 + M = HO_2 + M$ (R3) steps. In Warnatz's scheme,

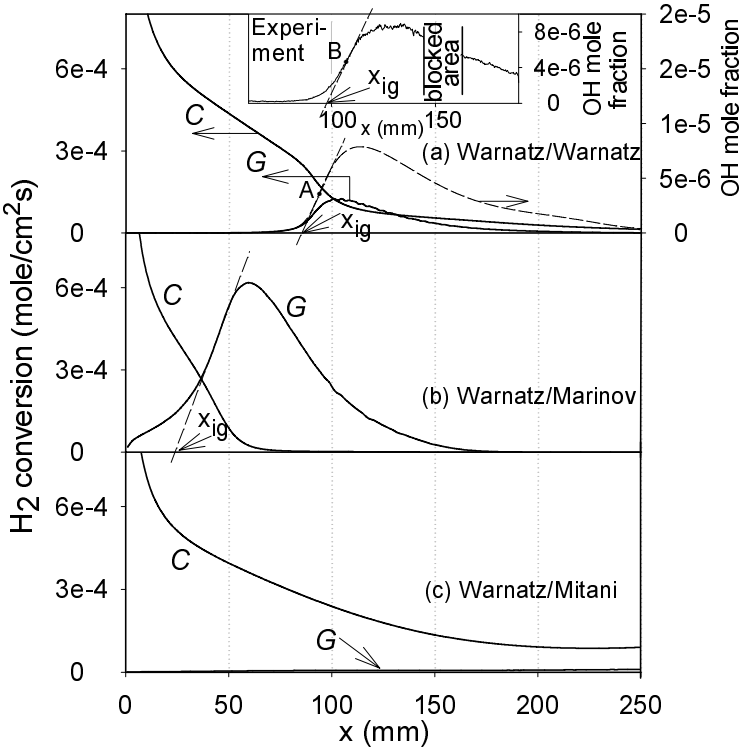

FIGURE 5 Catalytic (*C*) and gaseous (*G*) fuel conversion for case 4 of Table I. The definition of homogeneous ignition (x_{ig}) via the measured or predicted OH profiles is shown in panel a. In all predictions, the heterogeneous scheme of Warnatz was used (Table III). Predictions with the elementary gaseous scheme of Warnatz (panel a) are in good agreement with the measurements (inset of plate a). The one-step gaseous schemes, however, lead to either much earlier homogeneous ignition (see panel b) or no ignition at all (see panel c).

the multiplication factor of R3 was 1.2 and the division factor of R1 was 1.1. Warnatz's scheme ignited farther downstream (see Figure 4) and, therefore, had less amount of fuel available for gaseous combustion; an inhibition of homogeneous ignition through a decrease in R1 or increase in R3 by a factor of two, led to complete consumption of the fuel via the heterogeneous path and hence in no homogeneous ignition.

The Miller and Yetter schemes had (at any given *x*) the highest ratio R1/R3 (see Figure 7), leading to a faster radical pool build-up. This is also evident from the computed transverse profiles of the H, O, and OH radicals shown in Figure 8. In the near-wall region, the Miller and Yetter schemes had 2.0 to 3.5 times higher radical levels than those of Warnatz's scheme. The radical profiles of Figure 8 were dictated by the heterogeneous pathway. The O and H fluxes were always net-adsorptive, indicating that the catalyst was a sink for both radicals; this was a

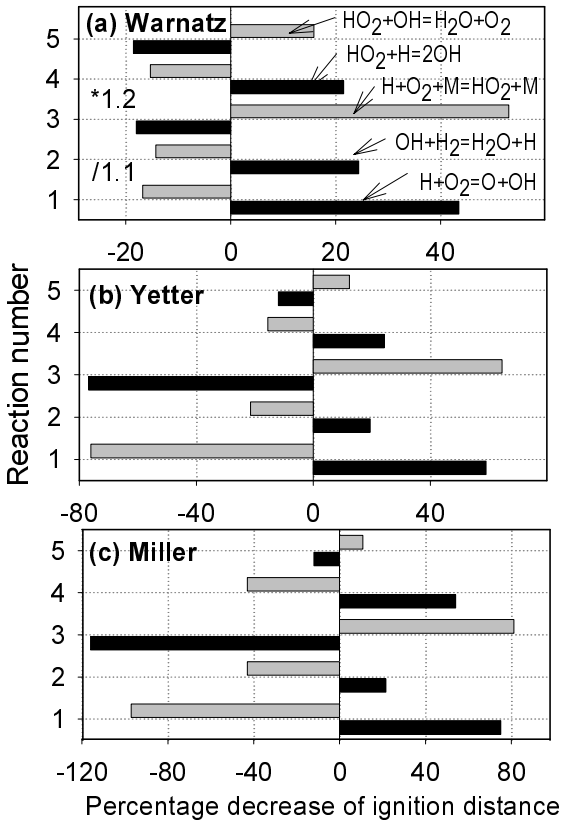

FIGURE 6 Sensitivity analysis on the elementary homogeneous schemes (and the heterogeneous scheme of Warnatz), case 3; all other cases have qualitatively similar responses. The black bars indicate the percentage decrease in homogeneous ignition distance (x_{ig}) for a reaction rate multiplication by a factor of two and the gray bars for a division by the same factor.

result of the absence of O and H desorption steps (their desorption was recombinative, see Table III). The OH fluxes were net-desorptive and the catalytic wall was a source of OH radicals. Nevertheless, this was not the case over the entire pre-ignition zone; at later distances the OH fluxes shifted to net-adsorptive. Hence, the catalytic wall was a sink of OH radicals at the latest pre-ignition stages. Overall, the OH heterogeneous pathway was an inhibitor of homogeneous ignition due to the increased importance of the latest pre-ignition stages. The heterogeneous radical inhibition will be discussed in the next section.

The differences between the predictions of the Yetter and Warnatz schemes are discussed next. These schemes had the same R1 reaction rate coefficients: therefore, their significant prediction differences pointed to an examination of the termination step R3. Water is a very efficient third body in R3 and significant

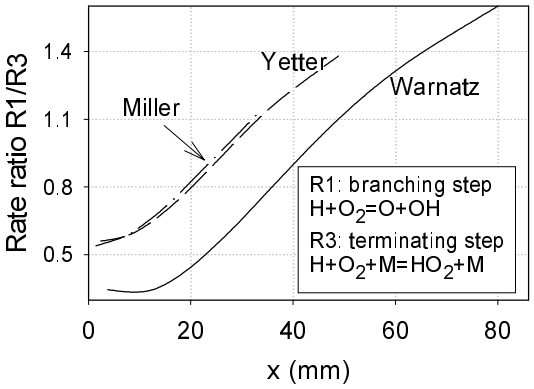

FIGURE 7 Streamwise rate ratio of the branching over terminating rates R1/R3, case 3; all other cases have qualitatively similar responses. Predictions with three homogeneous schemes and the heterogeneous scheme of Warnatz. The ratios refer to the transverse locations of maximum hydrogen production rate.

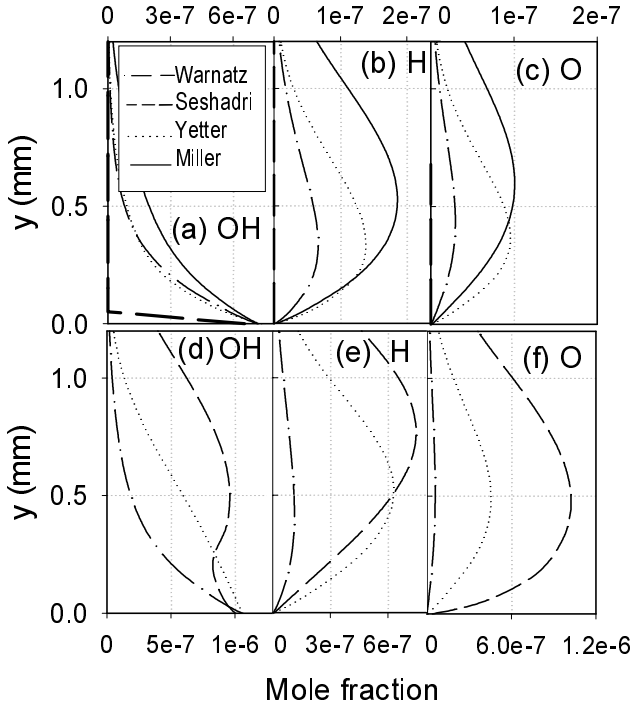

FIGURE 8 Predicted transverse profiles of the OH, H, and O mole fractions for case 4: (a), (b) and (c) refer to x = 18 mm. Predictions with the heterogeneous scheme of Warnatz and four homogeneous schemes; the radical levels with the reduced scheme of Seshadri are nearly zero. Plates (d), (e), and (f) refer to x = 32 mm for all homogeneous schemes except the scheme of Miller (already ignited in at this location, see Figure 4d).

amounts of it were produced via the heterogeneous pathway (~21% per volume near the wall as discussed in the forthcoming Figure 9). The third body efficiencies of water in R3, $\omega_3(H_2O)$, were artificially changed in the Warnatz and Yetter schemes from their respective values of 6.5 and 12 to the corresponding efficiencies of N_2 (0.4 and 1.0 respectively), and x_{ig} were recomputed. The ignition distances, for Case 4, were reduced to 33 mm (Warnatz) and 31 mm (Yetter) due to the decrease of the R3 rate, the reduction being much more pronounced in Warnatz's scheme; the x_{ig} differences between the two schemes were thus drastically reduced to about 6%. The presence of heterogeneously produced water provided, therefore, a plausible explanation for the discrepancies between the Warnatz and Yetter scheme predictions.

A similar procedure was used to investigate the large underpredictions of x_{ig} obtained with Miller's scheme. Setting $\omega_3(H_2O) = \omega_3(N_2) = 1.3$ resulted in x_{ig} = 14 mm, *e.g.*, the difference with Warnatz's scheme (33 mm) remained high. Hence, the presence of water was not the controlling factor for the significant underpredictions of Miller's scheme. Bengtsson (1998) studied NO_x formation in lean premixed methane/air combustion with comparative studies of various C/H/O/N schemes and reported consistent overprediction of NO_x with Miller's scheme; this was attributed to the entire H/O reaction subset that predicted a faster radical pool buildup. Replacing the R3 step in Miller's scheme with that of Warnatz's scheme, while keeping Miller's original water third-body efficiency, resulted in good agreement between the Warnatz and Miller predictions (within 8%). The present computations have thus shown that, under CST-relevant conditions, the radical pool was overpredicted in Miller's scheme, one possible reason being the underprediction of the terminating step R3.

The reduced scheme of Seshadri (in conjunction with Warnatz's heterogeneous scheme) yielded also large underpredictions of the measured ignition distance as shown in Figure 4e. It is noted that the elementary scheme of Warnatz was the one used in the reduction of Seshadri's scheme. The presence of heterogeneous adsorption/desorption reactions invalidated the steady state assumption of the O and OH radicals, which was used in the derivation of the reduced scheme: in the predictions with Warnatz's elementary scheme, for example, the local rate of gaseous OH destruction rate was about five times higher than the production rate over the entire pre-ignition zone. Although the radical levels in the Seshadri scheme were initially very low, (see Figures 8a–c at x = 18 mm), at x = 32 mm there were higher than those of the elementary schemes of Warnatz and Yetter (Figures 8d–f), resulting in the observed homogeneous ignition promotion.

The single-step mechanism of Marinov (in conjunction with Warnatz's heterogeneous scheme) yielded a much earlier ignition as illustrated by the early rise

of the gas-phase conversion profile of Figure 5b (85% underprediction of measured x_{ig}): the main reason was that all one-step schemes cannot account for the heterogeneous-induced radical inhibition. Finally, the one-step mechanism of Mitani yielded no homogeneous ignition (see the *G* profile of Figure 5c); The inability of reduced (including single-step) schemes to capture gas-phase ignition, exemplifies the need for the development of combined hetero/homogeneous reduced schemes that account properly for the chemistry coupling of both pathways.

Investigation of Heterogeneous Reaction Pathway

Figure 9 provides the Raman-measured transverse profiles of temperature, H_2 and H_2O mole fractions along with numerical predictions obtained with the Warnatz/Warnatz hetero/homogeneous schemes. The H_2 transverse profiles (both measured and predicted) indicate that the fuel conversion is practically mass-transport-limited throughout the entire pre-ignition zone. Comparisons between the computed H_2 profiles obtained with the three different heterogeneous schemes are illustrated in Figure 10 (purely heterogeneous computations). Notwithstanding small differences in the near-wall H_2 concentrations between the Schefer and the elementary-mechanism predictions (note also the logarithmic scale), the measured mass-transport-limited behavior was captured by all schemes. Given the fact that the catalytic pathway inhibits homogeneous ignition primarily via the near-wall fuel depletion, Figure 10 pointed that this inhibition mechanism was accounted for in all schemes.

For the two elementary heterogeneous schemes, a sensitivity analysis was performed in a fashion similar to that of the gas-phase mechanisms. The pre-exponential constants of every surface reaction were multiplied (divided) by a given

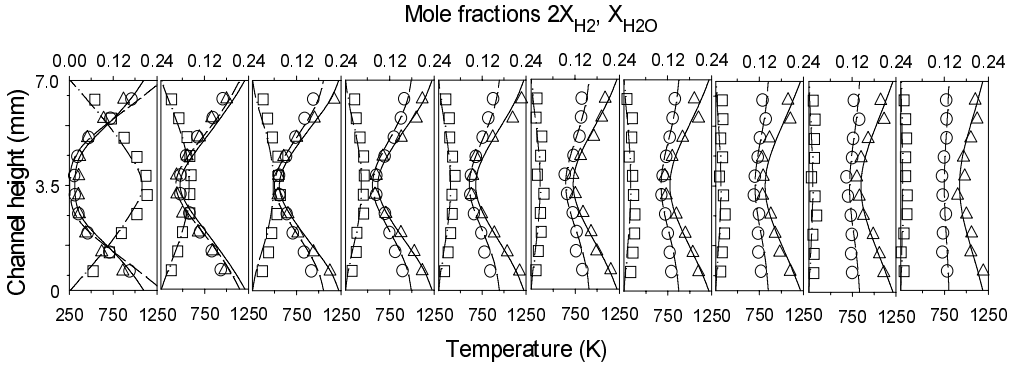

FIGURE 9 Raman-measured (symbols) and predicted (lines) transverse profiles of temperature and species (H_2 and H_2O) mole fractions in the catalytic channel at selected *x*-locations (from left to right: x = 25, 85, 105, 120, 135, 150, 165, 180, 195, and 235 mm), case 4. For reasons of clarity the H_2 mole fraction has been expanded by a factor of two. Squares: H_2, circles: H_2O, triangles: temperature. Dotted-dashed lines: H_2, dashed lines: H_2O, solid lines: temperature.

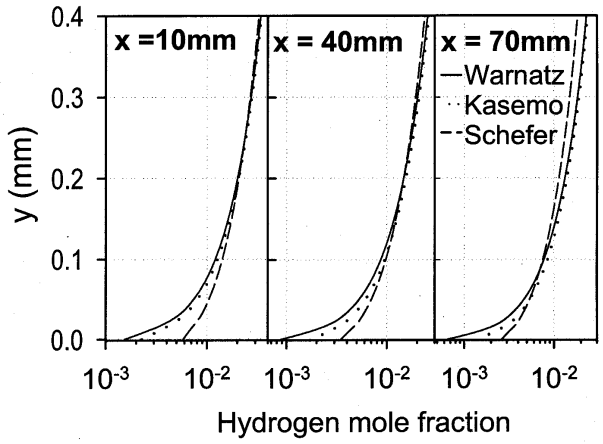

FIGURE 10 Transverse profiles of hydrogen extending 0.4 mm from the catalyst surface. Purely heterogeneous predictions with the three schemes of Table IV.

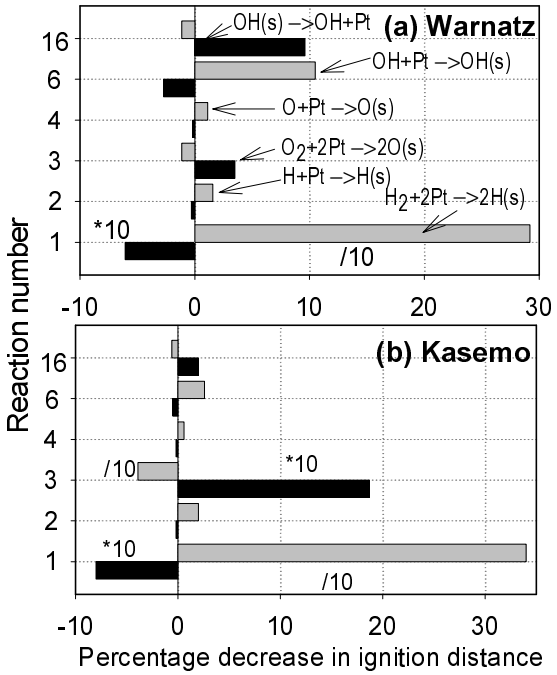

FIGURE 11 Sensitivity analysis on the elementary heterogeneous schemes (using the homogeneous scheme of Warnatz), case 3; all other cases had qualitatively similar responses. Percentage decrease in homogeneous ignition distance (x_{ig}) for a reaction rate multiplication (black bars) or division (grey bars) by a factor of twenty, unless otherwise indicated.

factor and the homogeneous ignition distances were recomputed; the homogeneous scheme of Warnatz was used in the heterogeneous sensitivity analysis. The results of this analysis are shown in Figure 11. The most sensitive reaction is, in both schemes, the hydrogen adsorption as it determines the near-wall fuel depletion. The highly skewed response of this reaction (see Figure 11) reflects the transport-limited fuel conversion; an increase of the H_2 adsorption rate by a factor of 10 does not alter significantly the H_2 boundary layer profiles of Figure 10, whereas a corresponding decrease by a factor of 10 shifts the H_2 adsorption to the kinetically controlled regime, resulting in a near-wall fuel excess that promotes substantially homogeneous ignition. Next in importance, but with significantly reduced sensitivity were (Warnatz's scheme) the OH adsorption/desorption reactions, the O and H adsorption reactions having minimal influence. However, it should not be erroneously concluded that the heterogeneous radical reactions could be safely removed in homogeneous ignition studies. Complete removal of the OH adsorption/desorption and of the O and H adsorption led, in Warnatz's scheme, to considerably earlier ignition (25% shorter x_{ig}) whereas removal of only the OH, O, and H adsorption reactions led to even shorter x_{ig} (by 45%). The above indicate that although the presence of the radical adsorption/desorption reactions was necessary in homogeneous ignition studies, the sensitivity analysis of Figure 11 has shown that accurate x_{ig} predictions can be accomplished even with large uncertainties in the corresponding kinetic parameters (radical sticking coefficients $0.05 < \gamma < 1$). The scheme of Kasemo had a large sensitivity on O_2 adsorption, contrary to Warnatz's scheme; this was due to the negative oxygen coverage dependence of the O(s) desorption activation energy (see reaction (14) in Table III) of the latter scheme. Although the radical adsorption reactions in Kasemo's scheme had smaller sensitivity compared to that of Warnatz's scheme, their presence was still necessary for homogeneous ignition: complete removal of the OH, O, and H reactions led to an earlier ignition by about 26%. Hence, the addition of these reactions to the original scheme of Kasemo was justified.

Having established the key heterogeneous reactions affecting homogeneous ignition, predictions with the different heterogeneous schemes are presented next. Kasemo's scheme yielded slightly shorter x_{ig} (by ~8%) compared to those of Warnatz's heterogeneous scheme. In that, Figures 4 and 5 remained essentially the same when the heterogeneous scheme of Warnatz was replaced with that of Kasemo. The reason for the good agreement was that both elementary heterogeneous schemes captured the measured mass-transport-limited fuel conversion and the radical adsorption inhibition.

Predictions with the one-step heterogeneous scheme of Schefer and four different homogeneous schemes are illustrated in Figure 12. Although the trend of

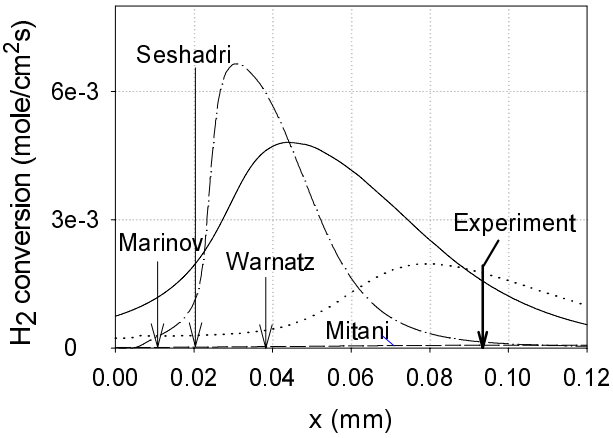

FIGURE 12 Predicted gas-phase fuel conversions with the heterogeneous one-step mechanism of Schefer and four different homogeneous schemes. Marinov: solid line, Seshadri: dotted-dashed line, Warnatz: dotted, Mitani: dashed.

increasing ignition distance in the order of Marinov–Seshadri–Warnatz–Mitani (the last scheme yielded no ignition) is preserved as in the predictions with Warnatz's heterogeneous scheme (see Figures 4 and 5), the absolute ignition distances were considerably shorter in the gaseous schemes of Warnatz and Seshadri. The reason was that the one-step heterogeneous description could not account for radical adsorption inhibition. An additional reason was the higher hydrogen near-wall levels obtained with this scheme (see Figure 10).

CONCLUSIONS

The applicability of various hetero/homogeneous chemical reaction schemes in the catalytically stabilized combustion of hydrogen-air mixtures over platinum was investigated experimentally and numerically in 2-D channel-flow configurations. Six homogeneous and three heterogeneous schemes (the scheme notation is given in Tables II and IV) were validated by comparing measured and predicted homogeneous ignition distances. Predictions with the elementary heterogeneous schemes of Warnatz and Kasemo (the latter augmented with the addition of adsorption reactions for the radicals O, H, and OH) yielded essentially the same ignition distances (within 8%), as both schemes were able to capture the mass-transport-limited fuel conversion and at the same time the ignition distance was insensitive to the magnitude of the radical adsorption/desorption kinetic parameters. Even though the sensitivity on radical adsorption/desorption was small, complete removal of these reactions reduced noticeably (by 26%) the ignition distance. The

one-step heterogeneous scheme of Schefer yielded much shorter ignition distances compared to the measured ones, as it lacked radical description and the catalytic fuel depletion rate was somewhat slower (compared to that of the elementary schemes) resulting in larger near-wall H_2 levels.

Three elementary homogeneous schemes (Warnatz, Yetter and Miller) were tested in conjunction with the elementary heterogeneous schemes of Warnatz and Kasemo. There were substantial differences between measured and predicted ignition distances. The best agreement was obtained with the gaseous scheme of Warnatz (8% underprediction). The schemes of Yetter and Miller resulted in large underpredictions (43% and 67% respectively): the large underpredictions of Yetter's scheme were attributed to the presence of heterogeneously produced water due to its effectiveness as third body in the chain terminating reaction $H + O_2 + M = HO_2 + M$, whereas the even larger underpredictions of Miller's scheme were attributed to a consistently higher radical pool buildup. The reduced scheme of Seshadri (reduction from the elementary scheme of Warnatz) underpredicted the measurements by 50% as the steady state assumptions for the OH and O radicals were invalidated in the presence of the heterogeneous radical pathway. Finally, the one-step gaseous mechanisms of Marinov and Mitani resulted in either much earlier ignition or no ignition at all. The failure of reduced heterogeneous or homogeneous schemes (and their combinations) to capture homogeneous ignition characteristics, exemplifies the importance of developing joint reduced hetero/homogeneous schemes where the coupling between catalytic and gaseous chemistries is properly accounted for. Such schemes can greatly aid the further development of catalytic combustors.

Acknowledgements

The Swiss Federal Office of Energy (BFE) and ALSTOM Switzerland provided support.

NOMENCLATURE

b	channel half-height
C_k	concentration of gas-phase species
D_{kl}	multicomponent diffusion coefficient
D_k^T	species thermal diffusion coefficient
E	activation energy
h	total enthalpy

K_g total number of gas-phase species
M_s total number of surface species
L channel length
Le Lewis number (thermal over species diffusivity)
p pressure
R universal gas constant
$\dot{s}_k$ species heterogeneous molar production rates
T temperature
U_{IN} inlet streamwise velocity
u, v streamwise, transverse velocity
$\vec{V}_k$ species diffusion velocity vector
$\dot{w}_k$ gas-phase species molar production rate
W channel width
W_k species molecular weight
$\overline{W}$ average mixture molecular weight
X_k gas-phase species mole fraction
Y_k gas-phase species mass fraction

Greek Symbols

γ_k sticking coefficient
Γ surface site density
Θ_m surface species coverage
λ thermal conductivity of the gas
μ viscosity
ρ density
σ_m surface species site occupancy
φ fuel-to-air equivalence ratio
$\omega_i(A)$ third-body efficiency of species A in reaction i

Subscripts

ig ignition
IN inlet
W wall

References

Aghalayam, P., Park, Y. K., and Vlachos, D. G. (2000). A Detailed Surface Reaction Mechanism for CO Oxidation on Pt. *Proc. Combustion Institute*, Vol. 28, pp. 1331–1339.

Appel, C., Mantzaras, J., Schaeren, R., Bombach, R., Inauen, A., Kaeppeli, B., Hemmerling, B., and Stampanoni, A. (2002). An Experimental and Numerical Investigation of Homogeneous Igni-

tion in Catalytically Stabilized Combustion of Hydrogen-Air Mixtures Over Platinum. *Combustion and Flame*, Vol. 128, pp. 340–368.

Beebe, K. W., Cairns, K. D., Pareek, V. K., Nickolas, S. G., Schlatter, J. C., and Tsuchiya, T. (2000). Development of Catalytic Combustion Technology for Single-Digit Emissions from Industrial Gas Turbines. *Catalysis Today*, Vol. 59, pp. 95–115.

Bengtsson, K. U. M., Benz, P., Schaeren, R., and Frouzakis, C. (1998). N_yO_x Formation in Lean Premixed Combustion of Methane in a High-Pressure Jet-Stirred Reactor. *Proc. Combustion Institute*, Vol. 27, pp. 1393–1399.

Bui, P. A., Vlachos, D. G., and Westmoreland, P. R. (1996). Homogeneous Ignition of Hydrogen/Air Mixtures over Platinum. *Proc. Combustion Institute*, Vol. 26, pp. 1763–1770.

Deutschmann, O., Schmidt, R., Behrendt, F., and Warnatz, J. (1996) Numerical Modeling of Catalytic Ignition. *Proc. Combustion Institute*, Vol. 26, pp. 1747–1754.

Deutschmann, O. and Schmidt, L. D. (1998). Modeling the Partial Oxidation of Methane in a Short-Contact-Time Reactor. *AIChE*, Vol. 44, 11, pp. 2465–2477.

Dobbeling, K. and Griffin, T. (1999). Method for Operating a Gas Turbine Group with Catalytic Gas Generator. Patent No. US5937632.

Dogwiler, U., Mantzaras, J., Benz, P., Kaeppeli, B., Bombach, R., and Arnold, A. (1998). Homogeneous Ignition of Methane/Air Mixtures over Platinum: Comparison of Measurements and Detailed Numerical Predictions. *Proc. Combustion Institute*, Vol. 27, pp. 2275–2282.

Dogwiler, U., Benz, P., and Mantzaras, J. (1999). Two-Dimensional Modeling for Catalytically Stabilized Combustion of a Lean Methane-Air Mixture with Elementary Homogeneous and Heterogeneous Chemical Reactions. *Combustion and Flame*, Vol. 116, pp. 243–258.

Hellsing, B., Kasemo, B., and Zhdanov, V. P. (1991). Kinetics of the Hydrogen–Oxygen Reaction on Platinum. *Journal of Catalysis*, Vol. 132, pp. 210–228.

Hickman, D. A. and Schmidt, L. D. (1993). Steps in CH_4 Oxidation on Pt and Rh Surfaces: High-Temperature Reactor Simulations. *AIChE*, Vol. 39, 7, pp. 1164–1177.

Kee, R. J., Dixon-Lewis, G., Warnatz, J., Coltrin, M. E., and Miller, J. A. (1996). A Fortran Computer Code Package for the Evaluation of Gas-Phase Multicomponent Transport Properties. Sandia Report SAND86-8246.

Kuijlaars, K. J., Kleijn, C. R., and van den Akker, H. E. A. (1995). Multicomponent Diffusion Phenomena in Multiple-Wafer Chemical Vapor Deposition Reactors. *The Chem. Eng. Journal*, Vol. 57, pp. 127–136.

Mantzaras, J. and Benz, P. (1999). An Asymptotic and Numerical Investigation of Homogeneous Ignition in Catalytically Stabilized Channel Flow Combustion. *Combustion and Flame*, Vol. 119, pp. 455–472.

Mantzaras, J., Appel, C., and Benz, P. (2000a). Catalytic Combustion of Methane/Air Mixtures over Platinum: Homogeneous Ignition Distances in Channel Flow Configurations. *Proc. Combustion Institute*, Vol. 28, pp. 1349–1357.

Mantzaras, J., Appel, C., Benz, P., and Dogwiler, U. (2000b). Numerical Modeling of Turbulent Catalytically Stabilized Channel Flow Combustion. *Catalysis Today*, Vol. 59, pp. 3–17.

Marinov, N. M., Westbrook, C. K., and Pitz, W. J. (1995). Detailed and Global Chemical Kinetics Model for Hydrogen. *8th Int'l Symp. on Transport Properties*, San Francisco, CA.

Miller, J. A. and Bowman, C. T. (1989). Mechanism and Modeling of Nitrogen Chemistry in Combustion. *Prog. Energy Combustion Science*, Vol. 15, pp. 287–338.

Mitani, T. and Williams, F. A. (1980) Studies of Cellular Flames in Hydrogen–Oxygen–Nitrogen Mixtures, *Combustion and Flame*, Vol. 39, pp. 169–190.

Mueller, M. A., Kim, T. J., Yetter, R. A., and Dryer, F. L. (1999). Flow Reactor Studies and Kinetic Modeling of the H_2/O_2 Reaction. *Int. Journal of Chemical Kinetics*, Vol. 31, pp. 113–125.

Pfefferle, W. C. and Pfefferle, L. D. (1985). Catalytically Stabilized Combustion. *Progress in Energy and Combustion Science*, Vol. 12, pp. 25–41.

Schefer, R. W. (1982). Catalyzed Combustion of H_2/Air Mixtures in a Flat Plate Boundary Layer: II. Numerical Model. *Combustion and Flame*, Vol. 45, pp. 171–190.

Seshadri, K., Peters, N., and Williams, F. A. (1994). Asymptotic Analyses of Stoichiometric and Lean Hydrogen-Air Flames. *Combustion and Flame*, Vol. 96, pp. 407–427.

Warnatz, J. and Maas, U. (1993). *Technische Verbrennung*, Springer-Verlag, Berlin, pp. 101–102.

Warnatz, J., Allendorf, M. D., Kee, R. J., and Coltrin, M. E. (1994). A Model of Elementary Chemistry and Fluid Mechanics in the Combustion of Hydrogen on Platinum Surfaces. *Combustion and Flame*, Vol. 96, pp. 393–406.